

# Angular-Scattering Characteristics of Ferroelectric Liquid Crystal Electro-Optical Devices Operating in the TSM and ESM Modes

Two optical effects in liquid crystals most frequently employed for light modulation applications include (1) electrically variable birefringence, which can be used to produce either phase modulation<sup>1,2</sup> or, if polarizers are employed, amplitude modulation;<sup>3-5</sup> and (2) field-induced scattering effects.<sup>6</sup> Although variable birefringence devices have received much greater attention in recent literature,<sup>1-5,7</sup> the inherent optical losses posed by the requirement for polarization optics make them less desirable for applications in which incident light energy is limited. One such application is in mid-infrared imaging systems that employ uncooled focal-plane-array detectors, which are comprised of a two-dimensional array of IR detectors, sensitive to radiation in the 8- to 14- $\mu\text{m}$  region, that are thermally isolated from their surroundings.<sup>8</sup> The detector material is selected to display a sharp change in its electrical properties (resistance, pyroelectric polarization, dielectric constant) with temperature. A frequently used example of such a material is the ferroelectric ceramic barium strontium titanate (BST). The individual detector array elements are read out sequentially by means of an electronically addressable array of readout cells connected to each detector. The detector signals are then multiplexed out of the focal plane for signal processing and display of a visible image of the thermal signature of the scene and targets. Since these focal-plane arrays operate near room temperature, only a single-stage, low-power thermoelec-

tric cooler is required to provide thermal stabilization. A simple mechanical chopper is the only moving part in systems using BST detector arrays. These systems are compact, lightweight, and highly reliable with low-power requirements since neither a complex mechanical scanner nor cryogenic cooling is required. Numerous applications in both the military and commercial sectors have been envisioned for this emerging imaging technology.

Development activities in uncooled focal-plane-array technology are currently driven by the need to achieve further reductions in size, weight, and power requirements without sacrificing performance.<sup>8</sup> One issue that has a relatively large impact on systems employing BST detector arrays is the requirement for a modulation device that enables the detector to see a change in temperature between the target scene and some background reference temperature. The current technology employs a rotating mechanical chopper containing a germanium disk with a series of lenslet arrays ground into its surface to alternately defocus (diffuse) and transmit the incident IR radiation. A simplified schematic representation of the BST focal-plane-array imaging device is shown in Fig. 72.20. Without the chopper in the system, only moving objects in the scene could be detected since, in the absence of a repeatedly refreshed background signature, the

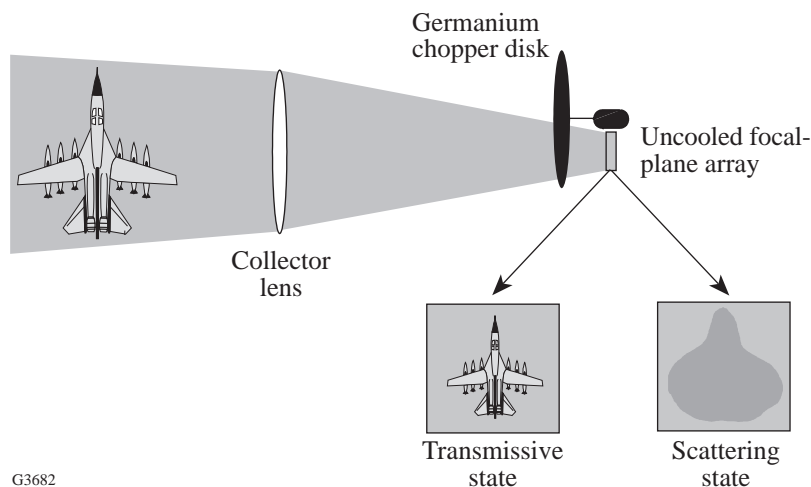


Figure 72.20  
A simplified schematic representation of an uncooled BST focal-plane-array imaging device. The motor-driven germanium chopper disk contains a series of lenslet arrays ground into its surface to alternately diffuse and transmit incident IR radiation.

detector surface charge would dissipate and cause the scene contrast to reduce to near zero. Replacement of the motor-driven mechanical chopper with a low-power, solid-state modulator that could be scaled to detector size would be a highly desirable technology-development option. Liquid crystal devices suggest themselves as an excellent alternative for this application by virtue of their low power consumption, short-path-length requirements, scalability of size, and excellent transmission characteristics in many regions of the near- and mid-infrared.<sup>1-7,9-12</sup> Modulation device concepts employing the cholesteric–nematic phase transition,<sup>9,10</sup> dynamic scattering,<sup>11</sup> and polymer-dispersed nematic liquid crystals<sup>12</sup> have been demonstrated; however, the long electro-optic relaxation times observed in these devices (100 ms to several seconds) are several orders of magnitude too slow to satisfy current requirements (<1 ms). A more promising approach uses the scattering produced by rapid field-induced unwinding of the helical structure in thick (10- to 100- $\mu\text{m}$ ) ferroelectric liquid crystal (FLC) devices in which the helix axis is oriented parallel to the substrates. This “transient-scattering mode” (TSM) device, first reported by Yoshino and Ozaki,<sup>13-18</sup> is shown in Fig. 72.21. The initial application of an electric field produces a highly transparent, helix-unwound state; the electric field polarity is then rapidly reversed, and the violent molecular motion that occurs as the ferroelectric LC domains align with the new field direction results in intense light scattering. The transmissive state is then restored as the helix once again

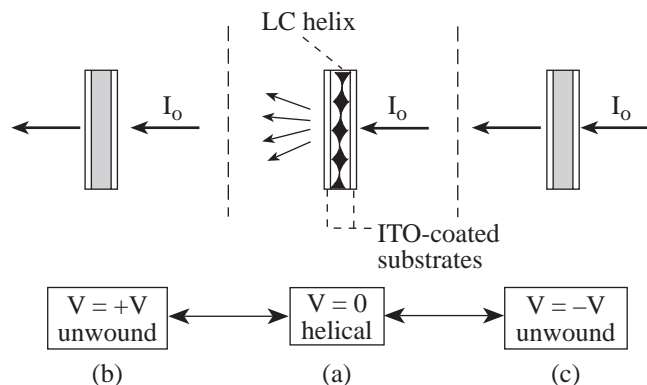


Figure 72.21  
 The transient-scattering mode in ferroelectric liquid crystals. (a) With no field applied, the helix axis lies parallel to the substrates, producing a weakly scattering texture; (b) application of a dc field causes the helix to unwind, rendering the cell highly transparent; and (c) a rapid reversal of dc field polarity and intense, transient light scattering occurs as the ferroelectric LC domains align with the new field direction.

becomes completely unwound and the new direction of spontaneous polarization is established. Rise and decay times ranged from tens to hundreds of microseconds,<sup>14</sup> depending on the magnitude of the drive voltage pulse and the cell thickness. More recently, Marshall *et al.*<sup>19</sup> demonstrated that it was possible to extend the duration of the scattering state to periods ranging from hundreds of microseconds to milliseconds in TSM devices by using specially designed waveforms that consisted of alternating polarity dc pulses superimposed upon a high-frequency ac signal. The ability of these “extended-scattering-mode” (ESM) devices to modulate radiation in both the visible and mid-infrared regions was verified in a simple experiment using an Fourier-transform infrared (FTIR) spectrometer, in which an unoptimized ESM device displayed a 40% modulation depth for IR radiation in the 8- to 12- $\mu\text{m}$  region.<sup>19</sup>

In this article, we expand on this previous work to examine the angular distribution of forward-scattered light by the field-induced unwinding of the helical structure in TSM and ESM ferroelectric LC devices. Such information on the distribution of forward-scattered light is important for the design of optical systems employing TSM or ESM devices, in that it gives an understanding of how close to the uncooled focal-plane-array detector the modulation device must be to ensure that the entire image fills the detector’s clear aperture. Although it would have been most desirable to conduct angular-scattering measurements in the mid-infrared for greatest relevance to the application of interest, our FTIR spectrometer was, by design, incapable of conducting measurements at any angle other than normal incidence. Because no other mid-IR detector was available to us, we instead conducted these measurements using an existing goniometer setup employing a visible-region light source.

### Angular-Scattering Distribution Measurements

Three FLC materials commercially available from Merck, Ltd.—ZLI-4139, ZLI-4003, and SCE-9—were evaluated using the goniometer test setup shown in Fig. 72.22. The beam from a 15-mW, linearly polarized, helium–neon laser was expanded and passed through a quarter-wave plate to produce circular polarization. We chose to use circularly polarized light in this work in order to observe the distribution of forward-scattered light without polarization effects. After propagating through the quarter-wave plate, the beam was collimated and allowed to pass through the FLC cell at normal incidence. A larger beam diameter ( $\approx 11$  mm) than in our previous work ( $\approx 1$  mm) was used to ensure that scattering was averaged over a large portion of the device’s clear aperture, thus allowing a

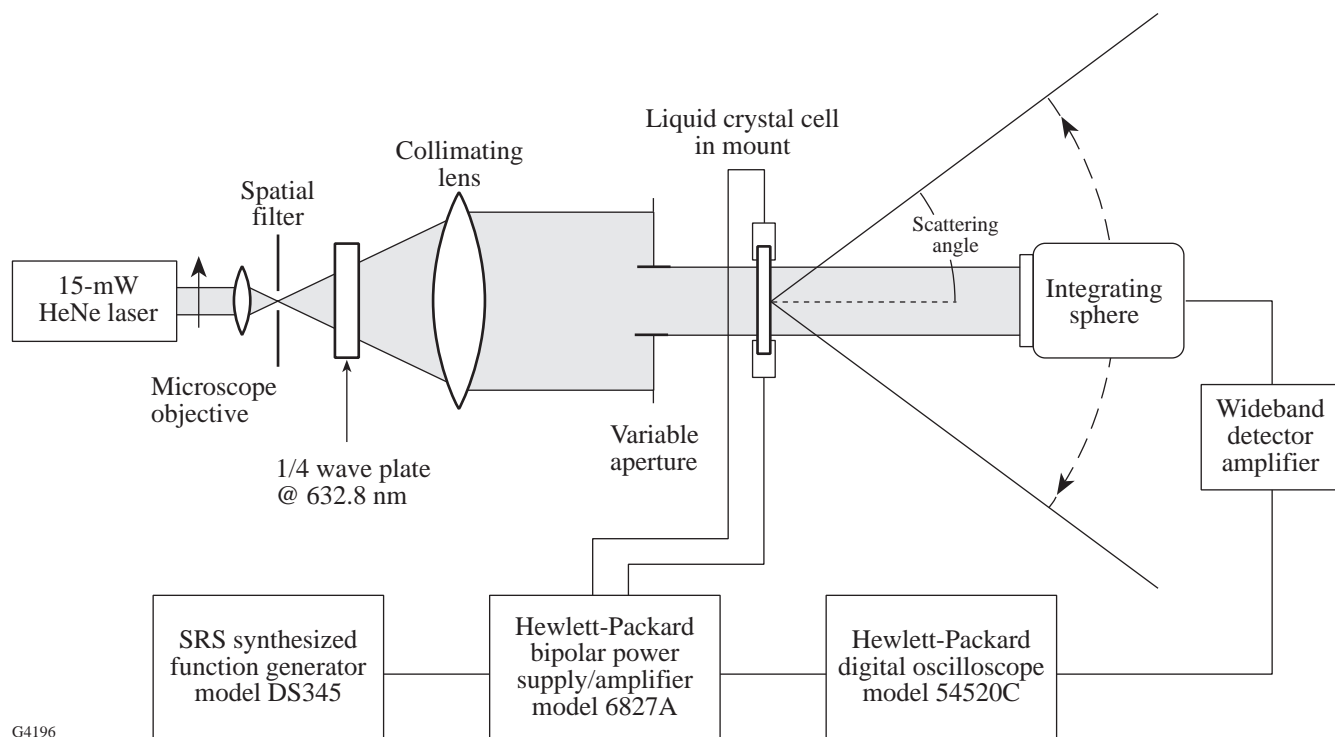


Figure 72.22

Diagram of the experimental setup used to measure angular scattering for ferroelectric LC devices operating in both the TSM and ESM modes. The integrating sphere can be rotated through an angle of  $\pm 60^\circ$ , about the normal to the FLC substrate surface.

more realistic evaluation of the device's behavior. The forward-scattered light was collected by an integrating sphere with a UDT PIN-10D photodiode. The integrating sphere was rotated about the normal to the cell substrate plane to determine the angular spread ( $\theta_s$ ) of the incident light out to  $20^\circ$ ; beyond this point the signal-to-noise ratios attainable with this setup were too small to allow reliable data.

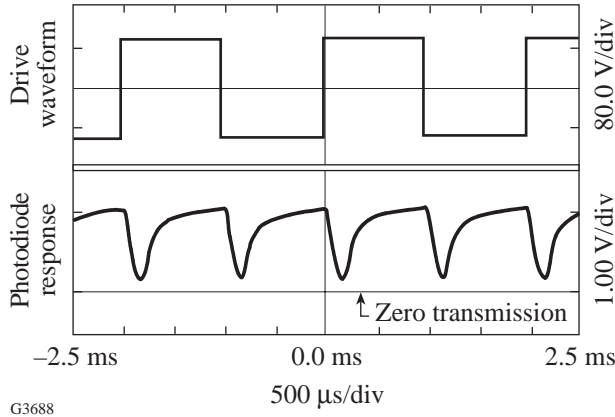
The FLC cells were driven with a Stanford Research Systems DS345 digital function generator connected to a Hewlett-Packard 6827A bipolar power supply/amplifier. The amplified signal was routed to a Hewlett-Packard 54520C digital oscilloscope to display the driving waveform. The integrating sphere detector was connected to a Melles Griot 13AMP005 wideband detector amplifier, which in turn is connected to the oscilloscope to display the output signal.

The cells evaluated in this study—SCE-9 (10  $\mu\text{m}$  and 24  $\mu\text{m}$ ), ZLI-4139 (10  $\mu\text{m}$  and 22  $\mu\text{m}$ ), and ZLI-4003 (24  $\mu\text{m}$ )—were assembled from glass substrates bearing a 500-Å, transparent, conductive ITO coating with a resistivity of 100  $\Omega/\text{square}$ . The substrates were spin coated with a 2-wt%

solution of nylon in formic acid, which, after being baked at  $115^\circ\text{C}$  for 1.5 h and then buffed, served as an alignment layer for the FLC. The coated substrates were oriented with their alignment layers parallel to each other, but with opposing rub directions, and then bonded together using Master Bond UV15-7TK1A UV curable epoxy mixed with 10-, 22-, or 24- $\mu\text{m}$  glass fiber spacers to control cell thickness. The cells were then heated above the clearing temperature of the FLC material's isotropic phase and filled by capillary action. To ensure homogeneous alignment of the FLC throughout the cell, we used a Mettler FP82HT Hot Stage to cool the cell very slowly ( $0.2^\circ\text{C}/\text{min}$ ), from the isotropic phase down to the ferroelectric  $S_c^*$  phase, while applying a 15- to 30-V, 0.1-Hz sine wave by means of a function generator. This step was most important for thicker cells ( $>20 \mu\text{m}$ ) and the short helical pitch materials (ZLI-4139 and ZLI-4003) to help ensure good alignment within the FLC devices. Prior to filling, the cell thickness was verified through an interference fringe counting method using a Perkin-Elmer Lambda-9 spectrophotometer.<sup>20</sup> These empty cells were shown to vary by less than 7% from the nominal spacer diameter. For consistency, all scattering response measurements were done at ambient temperature ( $22^\circ\text{C}$ ).

**TSM Angular Scattering**

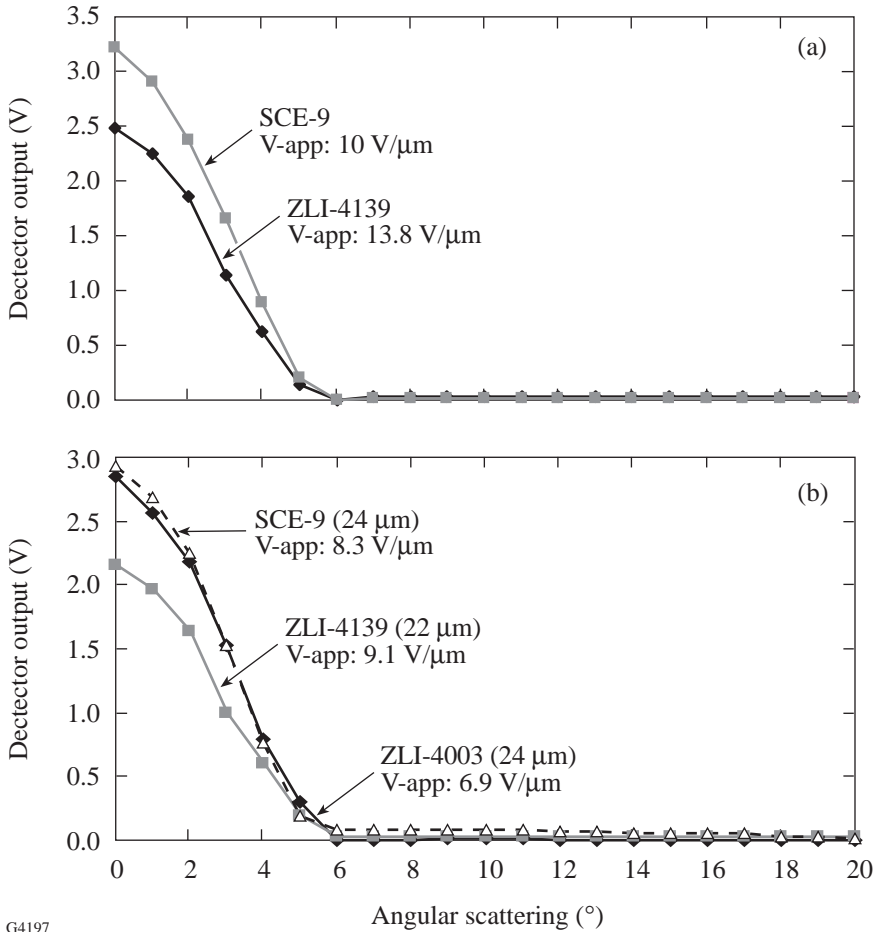
All TSM angular-scattering measurements were taken using a simple square wave as the driving waveform (Fig. 72.23). Similarly shaped plots were obtained for all of the devices



G3688

Figure 72.23 Electro-optical response of ZLI-4003 in the transient-scattering mode. The cell path length employed was 25  $\mu\text{m}$ .

tested when the photodiode output values were plotted over a 20° angular spread, as shown in Figs. 72.24(a) and 72.24(b). Since all evaluated devices displayed symmetrical scattering behavior about normal incidence, only one-half of the scattering envelope about normal incidence is shown in these and all subsequent figures for convenience. Each cell was driven at its optimum frequency and within its ideal voltage range [determined experimentally (at  $\theta_s = 0$ ) for each material/cell combination] to produce the greatest possible modulation depth. As shown in the figures, the bulk of the forward-scattered radiation falls within 6° of the normal and drops off sharply up to approximately 5°. Very little scattering is observed past 6°, which is in direct contrast to the behavior observed by both Tagawa *et al.*<sup>21</sup> and Kobayashi *et al.*,<sup>22</sup> who reported measurable scattering of the input beam at angles of up to 50°. One probable explanation is that the FLC cells used in these studies were one order of magnitude thicker ( $\approx 100 \mu\text{m}$ ) than the cells used in our study and thus would be expected to exhibit much stronger scattering behavior due to the increased path length. We were unable to verify this supposition because the voltage required to drive such long-pathlength TSM devices at their



G4197

Figure 72.24 (a) Angular-scattering behavior of 10- $\mu\text{m}$ -path-length SCE-9 and ZLI 4139 FLC cells operated in the TSM mode. The applied voltage per unit path length for each device is shown in the figure. (b) Angular-scattering behavior of SCE-9 (24- $\mu\text{m}$ ), ZLI 4139 (22- $\mu\text{m}$ ), and ZLI 4003 (24- $\mu\text{m}$ ) FLC cells in the TSM mode. The applied voltage per unit path length for each device is shown in the figure.

optimal response levels exceeded the output capabilities of our equipment. However, we can qualitatively compare scattering as a function of path length under non-optimal drive-voltage conditions in cases where the applied voltages per unit path length are of a similar magnitude. If we examine the data in Table 72.II, which shows the relationship between the magnitude of angular forward scattering on applied field, we see that for the 10- $\mu\text{m}$  and 22- $\mu\text{m}$  ZLI-4139 cells, both driven at nominally 6.8 V/ $\mu\text{m}$ , the thicker cell shows the greater amount of forward scattering in the 0°–6° range. A similar trend can also be seen from Table 72.II for the 10- $\mu\text{m}$  and 24- $\mu\text{m}$  SCE-9 cells, driven at applied field strengths of 7.5V/ $\mu\text{m}$  and 7.29V/ $\mu\text{m}$ , respectively.

The strength of the spontaneous polarization of the FLC material and its helical pitch length were both shown to

enhance temporal response in our earlier work with TSM and ESM devices, which prompted us to look for a similar relationship in these experiments with respect to the intensity of forward-scattered light. In Fig. 72.24(b), the forward-scattering response of 24- $\mu\text{m}$ -thick ZLI-4003, 24- $\mu\text{m}$ -thick SCE-9, and 22- $\mu\text{m}$ -thick ZLI-4139 cells, each driven at its own optimum frequency and voltage requirements, is compared. The SCE-9 cell, in which the FLC material has a spontaneous polarization of 33.6 nC/cm<sup>2</sup>, clearly scatters more strongly than do the ZLI-4003 and ZLI-4139 cells, in which the FLC materials have spontaneous polarization values of -20.2 nC/cm<sup>2</sup> and 13.8 nC/cm<sup>2</sup>, respectively. The helical pitch length of the FLC material, shown in our earlier work to have a marked effect on response times, appears to make little if any contribution to improving the intensity or angular spread of forward-scattered light. Although our previous work

Table 72.II: Angular-scattering response data obtained from FLC cells of various materials composition and path length operated in the TSM mode.

Material Path Length ( $\mu\text{m}$ ) Applied Field (V/ $\mu\text{m}$ )	SCE-9 10	SCE-9 10	SCE-9 24	SCE-9 24	ZLI-4139 10	ZLI-4139 10	ZLI-4139 22	ZLI-4139 22	ZLI-4003 24	ZLI-4003 24
Angle (°)	Detector output (V)									
0	1.516	2.312	1.969	2.562	1.562	2.141	1.453	1.719	1.719	2.328
1	1.344	2.140	1.766	2.328	1.422	1.906	1.344	1.610	1.562	2.219
2	1.109	1.719	1.429	2.008	1.125	1.531	1.094	1.312	1.219	1.891
3	0.734	1.289	0.867	1.321	0.688	1.031	0.812	0.953	0.781	1.297
4	0.367	0.555	0.469	0.750	0.359	0.562	0.406	0.500	0.406	0.625
5	0.070	0.148	0.078	0.141	0.062	0.125	0.109	0.156	0.094	0.188
6	0.031	0.023	0.078	0.086	0.078	0.000	0.312	0.312	0.062	0.000
7	0.031	0.039	0.062	0.078	0.109	0.031	0.312	0.312	0.062	0.031
8	0.031	0.039	0.062	0.078	0.094	0.031	0.312	0.312	0.062	0.031
9	0.031	0.031	0.055	0.078	0.062	0.031	0.312	0.312	0.062	0.031
10	0.023	0.023	0.055	0.062	0.062	0.031	0.312	0.312	0.062	0.016
11	0.023	0.023	0.055	0.062	0.062	0.031	0.312	0.312	0.047	0.016
12	0.023	0.023	0.031	0.055	0.062	0.031	0.312	0.312	0.047	0.000
13	0.023	0.023	0.031	0.055	0.062	0.031	0.312	0.312	0.047	0.000
14	0.023	0.023	0.023	0.047	0.062	0.031	0.312	0.312	0.047	0.000
15	0.023	0.023	0.023	0.031	0.062	0.031	0.312	0.312	0.047	0.000
16	0.023	0.023	0.016	0.031	0.031	0.031	0.312	0.312	0.047	0.000
17	0.023	0.023	0.016	0.031	0.016	0.031	0.312	0.312	0.047	0.000
18	0.023	0.023	0.008	0.016	0.016	0.031	0.312	0.312	0.031	0.000
19	0.023	0.023	0.008	0.016	0.000	0.031	0.312	0.312	0.016	0.000
20	0.016	0.023	0.008	0.016	0.000	0.031	0.312	0.312	0.016	0.000

illustrated that materials with the *shortest* helical pitch and largest spontaneous polarization were the most desirable for maximizing the speed of response, here we can see from Fig. 72.24(b) that the material with the *longest* helical pitch and the highest spontaneous polarization (SCE-9) shows the largest amount of forward scattering over the  $0^\circ$ – $6^\circ$  range. The ZLI 4003 cell, whose FLC material has the *shortest* helical pitch and a large spontaneous polarization, follows closely behind, while the ZLI4139 device, whose FLC material has a relatively weak spontaneous polarization and a moderate pitch length, shows the poorest performance of the group.

### ESM Angular Scattering

The ESM driving waveforms in these experiments were produced using Stanford Research System’s Arbitrary Waveform Generator (AWG) software running on a standard PC platform and downloaded via an RS-232 interface to the function generator. These ESM waveforms consisted of alternating-polarity dc pulses superimposed upon a high-frequency ac signal, which made it possible to modulate the incident light so as to produce nearly ideal square wave, optical output (Fig. 72.25). Several specially designed ESM waveforms from our previous studies were examined for their ability to modulate the incident light; those waveforms showing the best performance were used in this study. These waveforms were further optimized at the function generator after downloading by making real-time adjustments to the amplitude and frequency of the overall waveform while driving the device under investigation.

The angular-scattering data collected from ESM measurements, shown in Figs. 72.26(a), 72.26(b), and Table 72.III, show some significant variations from the TSM data in Figs. 72.24(a), 72.24(b), and Table 72.II. The same general trends observed in the TSM experiments with respect to forward-scattered intensity at different applied voltages, path length, spontaneous polarization, and helical pitch length were also observed in the ESM experiments. However, comparison of the TSM and ESM data for ZLI-4139 at  $10\ \mu\text{m}$  and  $10\ \text{V}/\mu\text{m}$  (Fig. 72.27) shows that the TSM mode produces a considerably higher degree of scattering than does the ESM mode within the  $0^\circ$ – $6^\circ$  angular range. Similar results were also observed for SCE-9 at  $24\ \mu\text{m}$ , in the TSM and ESM modes with comparable voltages per unit path length of  $7.3\ \text{V}/\mu\text{m}$  (Table 72.II) and  $7.1\ \text{V}/\mu\text{m}$  (Table 72.III), respectively. This finding is somewhat contradictory to our earlier investigations with TSM and ESM devices, in which there was little difference observed in the intensity of forward-scattered radiation

between the TSM and ESM modes of operation in the same device. One possible explanation may be that in these experiments the apparatus sampled a tenfold-larger area of the cell’s clear aperture than in our previous work. Cells that employed longer material path lengths and/or shorter helical pitch lengths are known to have a much stronger tendency to be multidomain and thus reduce the overall scattering response. We can see some evidence of this by looking at the results in Table 72.III for the  $24\text{-}\mu\text{m}$  ZLI-4003 cell, which has the shortest helical pitch length ( $-3\ \mu\text{m}$ ) and also shows the greatest variation in forward-scattered intensity between TSM and ESM modes. Another contributing factor may be that the ESM waveforms employed to obtain these results were those used in our earlier experiments and thus may require further optimization. Although some adjustment of the waveforms is possible after downloading to the function generator, this adjustment is limited to modifying only the frequency and voltage values of the entire waveform. Separate adjustments to the dc and ac components of the waveforms may provide comparable TSM and ESM performance.

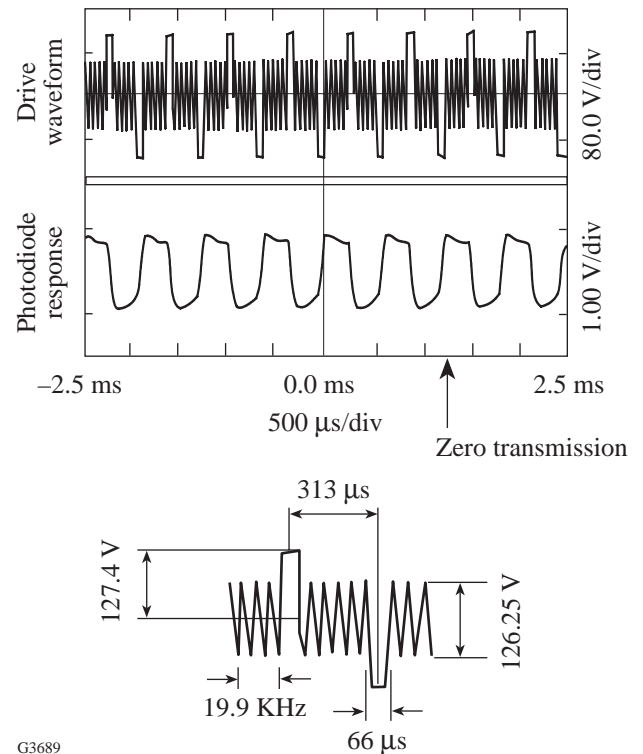


Figure 72.25 Electro-optical response of the  $25\text{-}\mu\text{m}$ -thick ZLI-4003 cell in the extended-scattering mode. An expanded view of the drive waveform used for the measurement is also included.

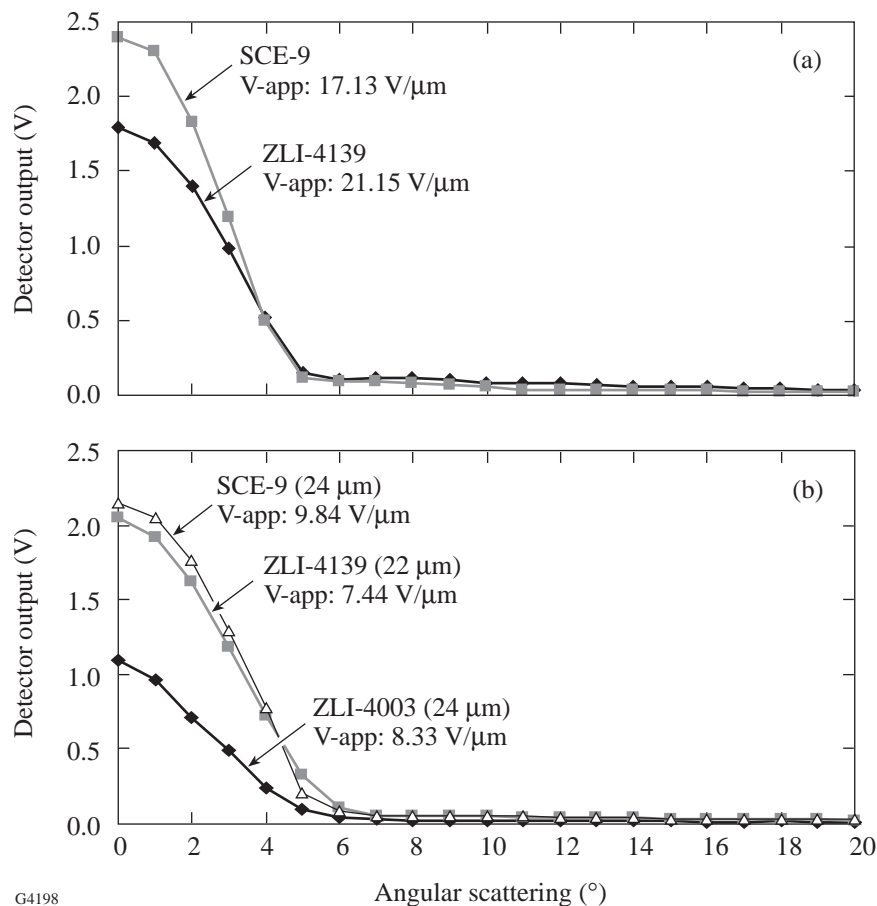


Figure 72.26  
 (a) Angular-scattering behavior of 10- $\mu\text{m}$ -path-length SCE-9 and ZLI 4139 FLC cells operated in the ESM mode. This data was obtained using the driving waveform shown in Fig. 72.25. (b) Angular scattering behavior of SCE-9 (24- $\mu\text{m}$ ), ZLI 4139 (22- $\mu\text{m}$ ), and ZLI 4003 (24- $\mu\text{m}$ ) FLC cells in the ESM mode.

G4198

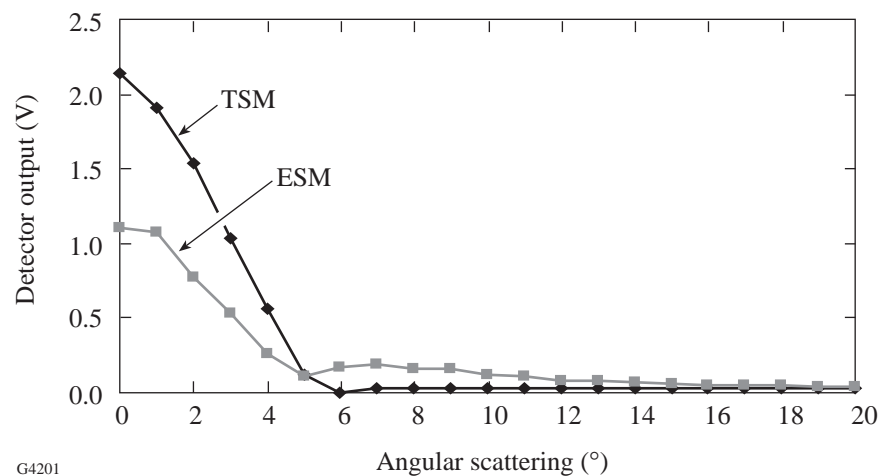


Figure 72.27  
 Comparison of angular-scattering behavior in the TSM and ESM modes for the 10- $\mu\text{m}$ -path-length ZLI 4139 cell. The same 10 V/μm applied field strength was used in both driving modes.

G4201

Table 72.III: Angular-scattering response data obtained from FLC cells of various materials composition and path length operated in the ESM mode.

Material	SCE-9	SCE-9	ZLI-4139	ZLI-4139	ZLI-4003
Path Length ( $\mu\text{m}$ )	10	24	10	22	24
Applied Field ( $\text{V}/\mu\text{m}$ )	10	7.1	10	7.4	8.5
Angle ( $^\circ$ )	Detector output (V)				
0	1.531	1.422	1.109	2.047	1.100
1	1.461	1.344	1.078	1.921	0.965
2	1.226	1.102	0.773	1.625	0.717
3	0.766	0.726	0.531	1.180	0.497
4	0.289	0.336	0.258	0.719	0.244
5	0.070	0.133	0.109	0.328	0.094
6	0.133	0.055	0.172	0.109	0.044
7	0.102	0.031	0.187	0.055	0.031
8	0.078	0.023	0.164	0.055	0.025
9	0.055	0.023	0.156	0.055	0.025
10	0.031	0.023	0.125	0.055	0.025
11	0.031	0.031	0.109	0.039	0.021
12	0.023	0.031	0.078	0.039	0.025
13	0.023	0.031	0.078	0.039	0.019
14	0.023	0.031	0.070	0.039	0.019
15	0.023	0.031	0.062	0.031	0.019
16	0.016	0.031	0.055	0.031	0.016
17	0.016	0.031	0.047	0.031	0.016
18	0.016	0.031	0.047	0.031	0.019
19	0.016	0.031	0.039	0.031	0.016
20	0.016	0.031	0.039	0.023	0.016

**Summary**

In this work, we have shown that the magnitude and distribution of forward-scattered light in FLC devices operating in the TSM and ESM modes are most greatly influenced by the device’s path length, the strength of the spontaneous polarization of the particular FLC material used in the device, and the operation mode—TSM or ESM. The helical pitch length, which was shown to have a large effect on the temporal response of TSM and ESM devices in our previous work, appears to have little or no effect on the magnitude or distribution of forward-scattered light in either mode of operation. Although there appears to be little difference in the angular distribution of forward-scattered light between the TSM and ESM modes, the TSM mode appears to produce more efficient

forward scattering over the  $0^\circ$ – $6^\circ$  measurable range of our experimental apparatus than does the ESM mode. These results indicate that additional work will be required before ESM devices can be employed as modulation devices in practical IR imaging systems employing uncooled focal-plane-array detectors. Of greatest importance is to obtain a much better understanding of the physical and optical mechanisms that are the underlying processes that govern the ESM effect. Only with a better working knowledge of these processes will it be possible to design driving waveforms and new FLC materials to better enhance angular scattering while at the same time maintaining the rapid temporal response required for mid-IR modulation applications.

## ACKNOWLEDGMENT

This work was supported in part by the Army Research Office under contract DAAL03-92-G-0147, the U.S. Department of Energy Office of Inertial Confinement Fusion under Cooperative Agreement No. DE-FC03-92SF19460, the University of Rochester, and the New York State Energy Research and Development Authority. The support of DOE does not constitute an endorsement by DOE of the views expressed in this article.

## REFERENCES

1. W. Gunning, J. Pasko, and J. Tracy, in *Imaging Spectroscopy*, edited by D. D. Norris (SPIE, Bellingham, WA, 1981), Vol. 268, pp. 190–194.
2. P. Joffre, G. Illiaquer, and J. P. Huguier, in *Electro-Optic and Magneto-Optic Materials and Applications*, edited by J. P. Castera (SPIE, Bellingham, WA, 1989), Vol. 1126, pp. 13–20.
3. S.-T. Wu and R. J. Cox, *Liq. Cryst.* **5**, 1415 (1989).
4. S.-T. Wu, *Opt. Eng.* **26**, 120 (1987).
5. Y. Shi, in *Optoelectronic Science and Engineering '90*, edited by D.-H. Wang (SPIE, Bellingham, WA, 1990), Vol. 1230, pp. 58–60.
6. V. A. Berenberg *et al.*, *Sov. J. Opt. Technol.* **60**, 487 (1993).
7. S.-T. Wu, U. Finkenzeller, and V. Reiffenrath, *J. Appl. Phys.* **65**, 4372 (1989).
8. R. E. Flannery and J. E. Miller, in *Infrared Imaging Systems: Design, Analysis, Modeling, and Testing III*, edited by G. C. Holst (SPIE, Bellingham, WA, 1992), Vol. 1689, pp. 379–395.
9. V. V. Danilov *et al.*, *Sov. J. Quantum Electron.* **15**, 1111 (1985).
10. J. G. Pasko, J. Tracy, and W. Elser, in *Active Optical Devices*, edited by J. Tracy (SPIE, Bellingham, WA, 1979), Vol. 202, pp. 82–89.
11. I. C. Khoo, Final Report #TCN 87-569, U.S. Army Research Office (1988).
12. J. W. McCargar, R. Ondris-Crawford, and J. L. West, *J. Electron. Imaging* **1**, 22–28 (1992).
13. K. Yoshino and M. Ozaki, *Jpn. J. Appl. Phys.* **23**, L385 (1984).
14. M. Ozaki and K. Yoshino, *Tech. Rep. Osaka Univ.* **35**, 53 (1985).
15. K. Yoshino *et al.*, *Jpn. J. Appl. Phys.*, Supplement 24-3, **24**, 59 (1985).
16. K. Yoshino and M. Ozaki, *Jpn. J. Appl. Phys.*, Supplement 24-2, **24**, 130 (1985).
17. M. Ozaki, S. Kishio, and K. Yoshino, *Mol. Cryst. Liq. Cryst.* **146**, 251 (1987).
18. K. Yoshino, M. Ozaki, and S. Kishio, *Jpn. J. Appl. Phys.*, Supplement 24-3, **24**, 45 (1985).
19. K. L. Marshall, S. D. Jacobs, and J. E. Miller, *Appl. Opt.* **34**, 6704 (1995).
20. I.-C. Khoo and S. T. Wu, *Optics and Nonlinear Optics of Liquid Crystals*, Nonlinear Optics, Vol. 1 (World Scientific, Singapore, 1993), p. 108.
21. A. Tagawa *et al.*, *Jpn. J. Appl. Phys.*, Supplement 28-2, **28**, 133 (1989).
22. J. Kobayashi *et al.*, *Mol. Cryst. Liq. Cryst.* **263**, 595 (1995).